Tracking Performance of Upgraded "Polished Panel" Optical Receiver on NASA's 34 meter Research Antenna

Victor Vilnrotter
Jet Propulsion Laboratory
4800 Oak Grove Dr.
Pasadena, CA 91109
818-354-4605
Victor.A.Vilnrotter@jpl.nasa.gov

Abstract—**There has been considerable interest in developing and demonstrating a hybrid "polished panel" optical receiver concept that would replace the microwave panels on the Deep Space Network's (DSN) 34 meter antennas with highly polished aluminum panels, thus enabling simultaneous optical and microwave reception[1]. A test setup has been installed on the 34 meter research antenna at DSS-13 (Deep Space Station 13) at NASA's Goldstone Deep Space Communications Complex in California in order to assess the feasibility of this concept. Here we describe the results of a recent effort to dramatically reduce the dimensions of the point-spread function (PSF) generated by a custom polished panel, thus enabling improved optical communications performance. The latest results are compared to the previous configuration in terms of quantifiable PSF improvement. In addition, the performance of acquisition and tracking algorithms designed specifically for the polished panel PSF are evaluated and compared, based on data obtained from real-time tracking of planets and bright stars with the 34 meter research antenna at DSS-13.**

TABLE OF CONTENTS

1. INTRODUCTION 1
2. MATHEMATICAL MODEL OF FOCAL-PLANE ARRAY PROCESSING.....2
3. INITIAL DATA ACQUISITION AND SIGNAL PRE-PROCESSING 5
4. IMPROVED PSF VIA PANEL MOUNTING UPGRADES 6
5. TRACKING ALGORITHM PERFORMANCE.....7
6. SUMMARY AND CONCLUSIONS 9
REFERENCES.....10

1. INTRODUCTION

The option to provide an optical communications capability for the 34-meter microwave antennas of the Deep-Space Network (DSN) is currently under consideration [1]. This concept is predicated on the assumption that existing RF capabilities would not be compromised, hence the new optical reception capability should be added without impacting the RF reflecting surfaces, the backup structure, or the pointing requirements on operational DSN antennas. One way to achieve optical communications requirements is to polish the aluminum panels of the antenna's main reflector to optical smoothness, and employ a suitably large detector array to collect the focused light. However, the extent to which thin aluminum panels can be shaped and polished to optical requirements remains to be quantified. This paper documents the results of recent experiments carried out at the Goldstone Deep Space Communications Complex (GDSCC), designed specifically to evaluate the suitability of polished aluminum panels for optical communications applications.

As a first step, two custom aluminum panels with prescribed curvature were procured from Vertex Antennentechnic, GmbH. (Germany), one of which was milled to a mirror-like surface while no special attempt was made to polish the other. A custom mounting bracket was constructed, and the polished panel mounted on the main reflector of the 34 meter antenna at DSS-13, as shown in Fig. 1. Note the shallow "grooves" produced by the milling process: these grooves were not removed by re-polishing after the milling operation, and impact the ability of this panel to form a small spot at optical frequencies. In the future, the second panel may be polished using a different technique to determine if a smoother optical surface can be obtained, and to characterize the potential gain that could be achieved by the improved surface quality. The location of the polished panel on the main reflector of the 34 meter antenna can be seen in Fig. 2a, near the entrance to the RF beam waveguide in the center of the main reflector.

In order to evaluate the spot size, or "point spread function" (PSF) generated by the polished panel at its prime focus, a 10 mega-pixel Finger Lakes Instruments (FLI) digital camera was installed in a weather-proof enclosure equipped with remote-controlled doors at each end for ventilation, mounted next to the subreflector on the movable part of the structure, and controlled from a small room located on the DSS-13 antenna called the "alidade".

[1] Author is with the Jet Propulsion Laboratory, California Institute of Technology. Copyright 2012 California Institute of Technology. Government sponsorship acknowledged.

978-1-4673-1813-6/13/$31.00 ©2013 IEEE

Figure 1. Polished aluminum panel manufactured by Vertex Antennentechnic, Germany, installed on the main reflector of the 34 meter antenna at DSS-13.

A picture of the mounted enclosure in the normally closed configuration is shown in Fig. 2b, tilted to point towards the center of the polished Vertex panel. The open configuration, used only during data-gathering, is shown in Fig. 2c where the 2" square narrowband optical filter assembly in front of the FLI camera can be seen. After installing the camera assembly and routing the control cable to the antenna's alidade, the camera enclosure was activated remotely and nominal operation of the entire system was verified.

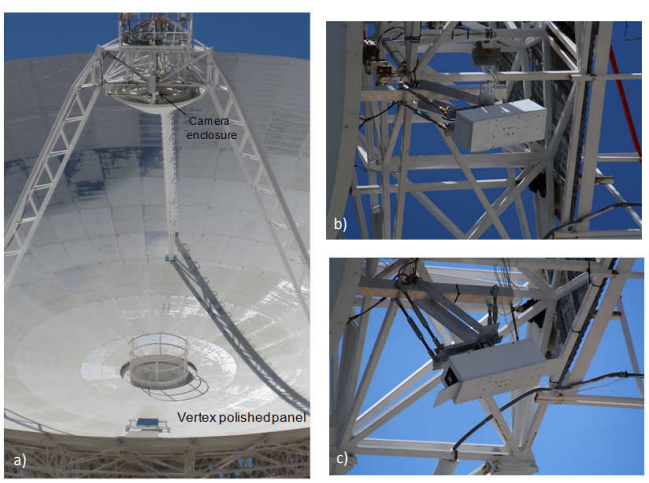

Figure 2. Vertex Polished Panel and FLI camera enclosure mounted on the 34 meter research antenna at DSS-13. a) Vertex polished panel mounted on the main reflector, close to the center; b) FLI camera enclosure mounted on the subreflector backup structure, closed configuration; c) FLI camera enclosure, open configuration.

The enclosure was designed to withstand desert heat, occasional heavy rain and wind with the aluminum doors closed as shown in Fig. 2b, and to quickly cool down during operation with both doors open (Fig. 2c). Although the assembly is always connected to AC power from the subreflector backup structure, the camera and all internal power supplies are activated via relays, which in turn are controlled remotely from the alidade via USB-2 extenders at each end connected via a durable CAT-5 cable running from the alidade through the main reflector and routed through the leftmost tripod leg in Fig. 2a.

2. MATHEMATICAL MODEL OF FOCAL-PLANE ARRAY PROCESSING

To facilitate analysis and derive the structure of the tracking algorithms, the sensor in the focal plane is modeled as an array of bins or pixels as shown in Fig. 3. Poisson distribution is assumed for the number of photo-electrons collected in each pixel in response to the signal intensity. The key features of the focal-plane model are defined in Fig. 3, which shows an elliptical intensity distribution, or PSF, in response to an optical point-source effectively at infinity such as the planet Jupiter or a bright star. The elliptical shape approximates the PSF generated by the Vertex panel after improvements were incorporated into the mounting structure, as described in Section IV.

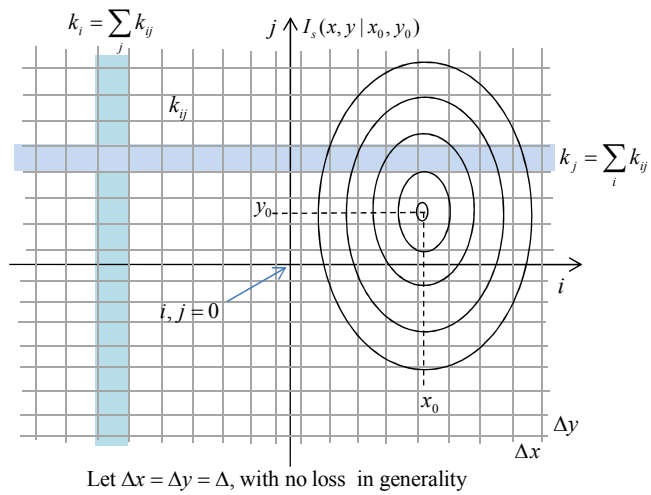

Figure 3. a) Focal-plane model of pixel array, and elliptical PSF with pointing offsets (x_0, y_0), motivated by experimentally determined point-spread function (PSF) for the high-quality Vertex panel.

For purposes of analysis, the PSF is assumed to be a two-dimensional elliptical Gaussian distribution with center at coordinates (x_0, y_0):

$$I_s(x, y \mid x_0, y_0) = I_s (2\pi \sigma_s^2)^{-1} \times \exp\{-[(x - x_0)^2 / 2\sigma_x^2 + (y - y_0)^2 / 2\sigma_y^2]\} \quad (1)$$

with units of watts/cm^2. The detector elements are small squares in this model, with power P_{ij} over the ij-th detector-element equal to the integral of the intensity distribution over its active area. Integrating power over

time yields energy, which can be converted to average "count-intensity" λ_s, where the received laser energy is measured in photo-electrons:

$$\lambda_s(i,j \mid x_0,y_0) = \int_0^T P_s(i,j \mid x_0,y_0)\,dt \cong T\Delta^2 I_s(i\Delta, j\Delta \mid x_0,y_0)$$

The photon count from the *ij*-th detector element over a time interval of T seconds can be modeled as a Poisson distributed random variable with count probability $p(k_{ij} \mid x_0,y_0) = [\lambda_s(i,j \mid x_0,y_0)]^{k_{ij}} \exp[-\lambda_s(i,j \mid x_0,y_0)]/k_{ij}!$, where k_{ij} is the observed photo-count from the *ij*-th detector element. Recognizing that counts from different detector elements are independent, and defining the count-vector from the entire array as $\mathbf{k} = [k_{ij}]$, the joint probability density of the array of counts becomes:

$$p(\mathbf{k} \mid x_0,y_0) = \prod_{i,j} [\lambda_s^0(i,j)]^{k_{ij}} \exp[-\lambda_s^0(i,j)]/k_{ij}! \qquad (2)$$

where we define $\lambda_s^0(i,j) \equiv \lambda_s(i,j \mid x_0,y_0)$ for notational convenience. Equation (2) is the starting point for deriving the maximum likelihood estimators for spatial acquisition, as well as for maximum likelihood detection of PPM symbols.

"Threshold-Centroid" Tracking Algorithm

As described in [1], the maximum likelihood estimator of the PSF offset coordinates in the absence of background can be determined by taking the natural logarithm of the conditional density defined in equation (2), and eliminating terms that contain no information about the signal coordinates:

$$\begin{aligned}\ln p(\mathbf{k} \mid x_0,y_0) &= \ln\left\{\prod_{i,j} [\lambda_s^0(i,j)]^{k_{ij}} \exp[-\lambda_s^0(i,j)]/k_{ij}!\right\} \qquad (3)\\ &= \sum_{i,j} k_{ij} \ln[\lambda_s^0(i,j)] - \sum_{i,j} \lambda_s^0(i,j) - \sum_{i,j} \ln(k_{ij}!)\end{aligned}$$

The last term is simply a constant, hence contains no information about the parameters of interest and can be ignored. Note that the likelihood function is the probability density of the count-array, conditioned on the PSF offsets (x_0,y_0). It is useful to define the total number of signal photons passing through the aperture in time T as

$$\begin{aligned}\sum_{i,j} \lambda_s^0(i,j) &= \int_0^T dt \sum_i \sum_j \int_{(i-1/2)\Delta}^{(i+1/2)\Delta} dx \int_{(j-1/2)\Delta}^{(j+1/2)\Delta} dy\, I_s(x,y \mid x_0,y_0)\\ &= \int_0^T dt \iint_{\substack{\text{detector}\\ \text{plane}}} I_s(x,y \mid x_0,y_0)\,dxdy = \Lambda_s \qquad (4)\end{aligned}$$

where the he total number of signal photons passing through the aperture in time T is $\Lambda_s = \sum_i \sum_j k_{ij}$. For a suitably large detector array, we can assume that the PSF is contained entirely within the array and contains no information about the PSF offset coordinates (x_0,y_0). Hence, for a large array, equation (3) can be simplified as:

$$\ln p'(\mathbf{k} \mid x_0,y_0) = \sum_{i,j} k_{ij} \ln[\lambda_s^0(i,j)] \qquad (5)$$

where "prime" indicates that this is no longer the natural logarithm of a valid probability density, but a simplified function that contains all the information needed to determine the PSF offsets, based on the observed photon-count array.

For acquisition and tracking applications, we need to determine those values of (x_0,y_0) that maximize the log-likelihood function defined in equation (5). The log-likelihood function is maximized by differentiating it with respect to the parameters of interest, setting the result equal to zero and solving, as described in [1]. This yields the following estimates, $(\hat{x}_0,\hat{y}_0)$, for the PSF offset coordinates:

$$\hat{x}_0 = \Delta \sum_i i\,k_i \Big/ \sum_i \sum_j k_{ij} \quad \text{and} \quad \hat{y}_0 = \Delta \sum_j j\,k_j \Big/ \sum_i \sum_j k_{ij} \qquad (6)$$

It can be seen that the maximum likelihood estimates of the offsets, $(\hat{x}_0,\hat{y}_0)$, are the centroids of the observed count-vectors, with k_i obtained by summing the counts along the index j (*y*-direction) for each index i (*x*-direction) as indicated in Fig. 3. A similar argument holds for estimating the *y*-coordinate of the PSF. This is the "best possible" estimator of the *x* and y coordinates when the statistics are Poisson, background photons are negligible and the detector array is large enough to contain the entire PSF.

The derivation for the case of finite detector arrays and background radiation becomes significantly more complex, as described in [1]. It was found that a modified version of the centroid algorithm that employs only those counts above a predetermined thresholds generates good results, since in effect it applies the centroid algorithm to only those regions where the PSF is large, and effectively eliminates the background intensity without the need to subtract a random estimate, which was found in [1] to degrade performance. This approach works well for the case where the integration time is long enough to generate an accurate estimate of the average PSF plus constant background intensity, so that the threshold can be set a few standard deviations above the average background but well below the peak of the elliptical Gaussian PSF. The form of this modified tracking algorithm, from now on referred to as the "threshold-centroid" algorithm, can be expressed as follows:

$$\hat{x}_0^* = \Delta \sum_i i\, k_i^* \Big/ \sum_i \sum_j k_{ij}^*$$
$$\hat{y}_0^* = \Delta \sum_j j\, k_j^* \Big/ \sum_i \sum_j k_{ij}^* \tag{7}$$

where k_{ij}^* refer to counts from those pixels exceeding a pre-determined threshold η, and k_i^* and k_j^* likewise refer to the sum of pixel counts only from those pixels exceeding the threshold along the *j* and *i* directions, respectively. Note that thresholding the pixel counts also helps to mitigate errors due to irregular background, resulting from unwanted light seeping through the gaps of the main reflector, as described in Section IV, or distortions and asymmetries on the tail of the PSF due to coma or other artifacts. However, some of the signal energy is lost due to the thresholding operation, which tends to increase the variance of the centroid estimates. This is the form of the algorithm we shall use to evaluate the potential tracking performance of the Vertex polished panel mounted on the main reflector of the 34 meter antenna at DSS-13.

Approximate Lower Bound

It was shown in [1] that for an infinite detector array and negligible background, the minimum attainable variance of the coordinate estimates are given by the Cramer-Rao bounds

$$\mathrm{var}(\hat{x}_0 - x_0) \geq \left\{ -E\left[-\sum_i \sum_j k_{ij} / \sigma_x^2 \right] \right\}^{-1} = \frac{\sigma_x^2}{\Lambda_s} \tag{8a}$$

$$\mathrm{var}(\hat{y}_0 - y_0) \geq \left\{ -E\left[-\sum_i \sum_j k_{ij} / \sigma_y^2 \right] \right\}^{-1} = \frac{\sigma_y^2}{\Lambda_s} \tag{8b}$$

where $\Lambda_s = E\sum_i \sum_j k_{ij}$ is the expected value of the total signal energy collected by the detector array. It is apparent that the variance of the coordinate estimate for each dimension is directly proportional to the variance of the PSF along the given dimension, namely σ_x^2 and σ_y^2, and inversely proportional to the average number of signal photons impinging on the detector array. This derivation assumes an infinite detector array, and a two-dimensional Gaussian PSF as described in [1]. For our application, we observe that if the detector array is significantly larger than the extent of the PSF, with the threshold set a few standard deviations above the expected noise counts, effectively eliminating the contribution of background noise, but not so high as to significantly truncate the low-intensity portions of the PSF, then it is reasonable to approximate the thresholded output as a zero-background model, with an approximately two-dimensional Gaussian PSF but with correspondingly reduced signal energy. This model suggests replacing the total signal energy Λ_s in equations (8) with the thresholded signal energy $\Lambda_s^* \equiv E\sum_i \sum_j k_{ij}^*$, where, as before, k_{ij}^* are the counts from pixels exceeding the threshold η. Under the above conditions, the lower bound on the variance of the estimation error for the threshold-centroid receiver may be approximated as

$$\mathrm{var}(\hat{x}_0^* - x_0)_{thresh} \geq \frac{\sigma_x^2}{\Lambda_s^*}$$
$$\mathrm{var}(\hat{y}_0^* - y_0)_{thresh} \geq \frac{\sigma_y^2}{\Lambda_s^*} \tag{9}$$

Note that $\Lambda_s > \Lambda_s^*$, hence $\mathrm{var}(\hat{x}_0^* - x_0)_{thresh} > \mathrm{var}(\hat{x}_0 - x_0)$ and $\mathrm{var}(\hat{y}_0^* - y_0)_{thresh} > \mathrm{var}(\hat{y}_0 - y_0)$. In other words, the threshold-centroid estimator, with less than the total signal energy to work with, always performs worse than the classical centroid estimator operating in the absence of background, and utilizing all of the available signal energy. Nevertheless, in many applications where the background energy over each pixel is not too great, so that a low value of threshold can be maintained (set just high enough to eliminate most of the random background counts), this approximation provides a useful estimate of the threshold-centroid algorithm's performance.

Symbol Error Probability Calculations

Assuming that the intensity distribution obtained from the camera is a reasonable representation of the average PSF generated by the Vertex polished panel, we proceed to evaluate communications performance for pulse-position modulation (PPM) with *M* slots per symbol. As described in [1], detector array processing can be optimized to achieve best performance by sorting the array elements according to pixel energy, and first computing the symbol error probability (PSE) for the highest energy detector element, then for the sum of the signal energies in the first two highest energy detectors, and so on, until the minimum PSE is reached. The amount of signal energy collected by the first "*m*" highest-energy detectors is denoted by

$$K_s(m) = \sum_{n=1}^{m} \lambda_s(n) \tag{10}$$

where "*n*" is the order index according to signal energy in descending order. If the background photons are uniformly distributed in the detector-plane, the amount of collected background energy increases linearly with *m* as more detector elements are included, and hence the average number of background photons collected by *m* detector elements is proportional to *m*, $K_b(m) = m\lambda_b$, where λ_b is the average background photon-count rate per detector

element, here assumed to be constant over the entire detector array.

As described in [1, 2], the symbol error probability, $P_M(E)$, can be well approximated by using a matched Gaussian density instead of the true Poisson density, which however leads to time-intensive computations. The Gaussian formula replaces the Poisson probabilities with continuous Gaussian densities whose second-order statistics have been matched to the Poisson distribution, yielding the following approximate expression for the probability of correct detection [3]:

$$P_M(C) \cong \int_{-\infty}^{\infty} dy\, Gsn[K_s(m)+K_b(m), y] \left[\int_{-\infty}^{y} dx\, Gsn[K_b(m), x] \right]^{M-1} \quad (11)$$

Here $Gsn(K, x)$ refers to the Gaussian density of the random variable x with mean and variance K. This approximation yields a somewhat pessimistic evaluation of optical receiver performance, but it is accurate for the high-signal high-background case we are considering in this paper. In the following sections, these concepts will be applied to determine the minimum probability of symbol error with PPM signaling, using the experimentally determined PSF to generate the signal distribution over a hypothetical photon-counting detector array.

3. Initial Data Acquisition and Signal Pre-Processing

Data collected during initial Jupiter observations on September 8th, 2011, consisted of files with 3084×3103 array elements, quantized to 16 bits. The control software of the FLI camera thresholds the pixel values at approximately 2000 out of a total of $2^{16} = 65536$, in order to overcome thermal current and other instrumental effects. Photo-electrons generated by the signal are added directly, generating the "salt-and-pepper" appearance of the original 10 mega-pixel image as can be seen in Fig. 4a, due to the Poisson nature of the photon-counts which are subject to significant fluctuations from one pixel to the next [2]. In order to eliminate the "salt-and-pepper" appearance of the high-resolution image, the pixels were binned into 60×60 pixel subarrays resulting in a 50×50 element array where the threshold value was subtracted before binning, hence the binned intensities shown in Fig. 4b now start at zero instead of 2000. No critical information is lost during the binning operation since the extent of the PSF is much greater than the size of the bins, hence the PSF is sampled adequately in both spatial dimensions. Upon closer inspection of the data, it was noted that the first row and first column of the array contained much less signal energy than the rest, hence the first row and column were deleted in subsequent processing resulting in a $49 \times 49 = 2401$ element array. This smaller array is much easier to process than the original 10 mega-pixel array, while retaining the information needed to characterize the PSF and evaluate optical tracking and communications performance.

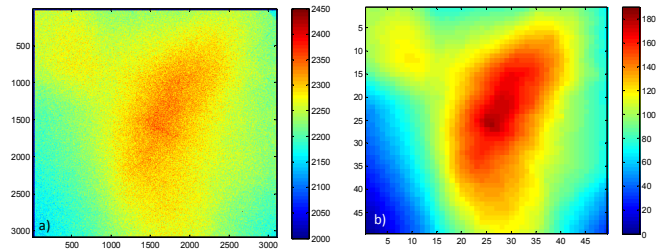

Figure 4. Centered PSF recorded by FLI camera: a) original 10 mega-pixel resolution showing "salt and pepper" pattern; b) smoothed 60X60 binned image showing the spatially averaged structure of the point-spread-function.

When the detector elements are sorted according to signal energy, the distribution of energies shown in Fig. 5a is obtained as a function of the order index "n". Note that all of the $49 \times 49 = 2401$ detector elements contain some signal energy, falling off with increasing order index n due to sorting.

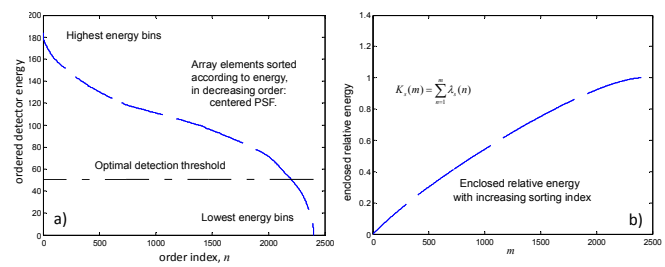

Figure 5. a) Detector elements sorted according to energy, for a centered PSF; b) accumulated relative energy in the first "m" sorted detector elements.

From the viewpoint of optical communications, the most important criterion is detecting and decoding the transmitted data with the highest possible fidelity. This implies the use of advanced detection strategies to achieve the lowest possible symbol-error probabilities consistent with the prevailing operating conditions. As shown in [3], optimum processing of photon-counting detector array data requires weighting of the array elements by a logarithmic factor that depends on the average signal and background energies over each pixel, which may be difficult to compute and apply in a practical implementation when a large number of detector elements are involved. However, it was also shown in [3] that a simple (1, 0) mask that selects the most favorable detector elements and rejects the rest achieves very nearly the same performance as the more complicated logarithmic weighting strategy. We shall proceed to analyze the symbol-detection capabilities of a hypothetical optical receiver by applying the optimum (1, 0) mask to a photon-counting array corresponding to the binned subarrays of the large-sensor FLI camera.

4. IMPROVED PSF VIA PANEL MOUNTING UPGRADES

When the initial data was collected and analyzed, it was determined that significant panel tilt and distortion were present. After this problem was corrected, a dramatic improvement in the shape of the PSF was observed, as can be seen in Fig. 6b (data recorded on February 16th, 2012). The signal energy has now been concentrated into a much smaller nearly bell-shaped PSF, as would be expected from a panel with excellent surface figure, but with considerable small-scale surface irregularities which prevent diffraction-limited performance at optical frequencies.

It was noticed in post-processing that the Jupiter PSF image shown in Fig. 6b had some unexpected horizontal streaks in the lower left, near coordinates (12, 27) and (12, 32). This was not noticed in the much fainter real-time images displayed by the camera in the field, hence no action was taken to correct the problem during the track. This was later attributed to light seeping through gaps in the main reflector from the control room, which was directly behind Jupiter during this track: this problem was eventually resolved and did not impact future tracks. Despite the interference by ground-lights in the Jupiter PSF, it was decided to use this Jupiter data for the following analysis, because a comparable Jupiter data-set was also available, taken before the polished panel upgrades were implemented, enabling meaningful comparison of the data.

Since the visual magnitude of Jupiter has decreased significantly between September 8th 2011 (when the initial Jupiter PSF was characterized) and February 16th 2012 when the latest data was collected, it was necessary to correct the measured intensities before any quantitative conclusions could be drawn. Each integer increase in visual magnitude decreases the source intensity by a factor of $\sqrt[5]{100} = 2.512$, hence a change of Δm_v in visual magnitude results in a corresponding change of $2.512^{\Delta m_v}$ in observed signal energy. The visual magnitude of Jupiter increased from -2.725 on September 8th 2011, to -2.25 by February 16th 2012, i.e. Jupiter was fading in February relative to September. The change in magnitude between September and February is $\Delta m_v = -2.25 - (-2.725) = 0.475$, which represents a decrease in Jupiter intensity by a factor of $2.512^{\Delta m_v} = 1.55$. This difference in brightness must be taken into account when comparing data recorded on different dates.

It can be seen in Fig. 6c that the maximum pixel intensity has more than doubled as a result of the recent panel structure upgrades (from 155 intensity-units to approximately 440), and the total signal energy has increased by a factor of 1.38, from the initial configuration (Fig. 6d).

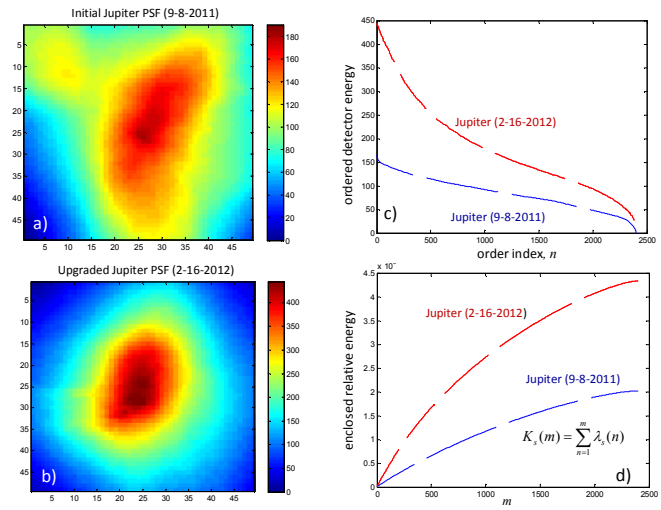

Figure 6. Comparison of point spread functions generated by the initial and upgraded panel mounting structures: a) Jupiter PSF obtained initially on 9/8/2011; b) improved Jupiter PSF after implementing upgrades to the panel mounting structure (2/16/2012); c) performance improvement quantified in terms of ordered detector energies; d) increased signal energy as a function of *m* due to better light concentration by the upgraded panel mounting structure.

After accounting for the decrease in Jupiter intensity by a factor of 1.55 between September 8th 2011 and February 16th 2012, the total increase in signal energy due to the upgrades in the polished panel mounting structure amount to a factor of 2.14 in total signal energy captured by the array.

Next, the error probability performance of the improved panel is compared with the previous configuration, using only the shapes of the PSF and the ratio of total signal energies to compute the symbol error probabilities for PPM symbols as a function of *m*, as described above. When the collected signal energy is distributed according to the Jupiter PSF shown in Fig. 7a, the difference in error probability performance is truly astounding: whereas the minimum symbol error probability reached by the original PSF depicted in Fig. 6a is only $PSE = 0.033$ for an assumed total signal energy of 70 photons over the entire detector array, the minimum error probability reached by the upgraded PSF, with $1.55 \times 1.38 = 2.14$ times the total signal energy of 150 signal photons distributed as in Fig. 6c, is much lower, namely $PSE = 5.8 \times 10^{-5}$. The optimum (1, 0) mask that achieves the minimum error probability is shown in Fig. 7a as the dark-blue "excluded region", passing only the fraction of the signal energy in the "included region" to the detection algorithm. This form of spatial filtering limits background radiation, while allowing the optimum amount of signal energy to contribute to the symbol decision.

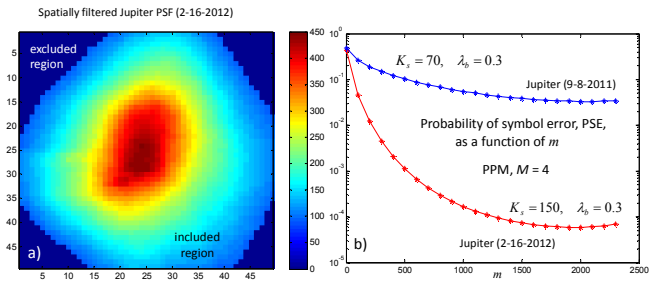

Fig. 7. PPM detection performance of the original panel configuration and the new, upgraded panel mounting structure. a) optimum (1, 0) mask for the upgraded PSF with 0.3 background photons per pixel; b) comparison of symbol-error probabilities for PPM with M = 4, after accounting for the difference in signal-energy concentration due to the improved panel, and for the change in Jupiter brightness between the data-sets.

Note that the average background count of 0.3 photons per pixel assumed in this example actually represents a very high background environment, since the total background energy over all 2401 pixels is $2401 \times 0.3 = 720$ photons. Therefore, this communications example actually represents a high background scenario even more stressful than would normally be encountered during routine daytime optical communications operations.

5. Tracking Algorithm Performance

The "threshold-centroid" algorithm described earlier was used to estimate the coordinates of the PSF in the following examples. Briefly, this tracking algorithm sorts the PSF pixel energies from highest to lowest, and computes the centroid of the pixel energies above a user-defined threshold applied to the image.

Several targets were tracked on February 16th, 2012, in addition to Jupiter which was then at an elevation of approximately 50 degrees, including Venus (setting, at an elevation of about 15 degrees), the brightest star Sirius, and the brightest star in the constellation Orion, Betelgeuse. As can be seen in Fig. 8, the PSF generated by Venus and the two stars now appear to be bell-shaped, with a hint of ellipticity and coma due to a slight residual panel misalignment. The white asterisk near the peak of each PSF is the threshold centroid algorithm's estimate of the peak, which seem to be in good agreement with visual inspection in all cases. As described earlier, the PSF generated by Jupiter shows significant asymmetry on the left side: this was found to be caused by distant lights on the ground seeping through the gaps between the antenna panels, and entering the camera directly instead of being reflected off the polished panel. However, this interference did not affect the performance of the tracking algorithm, since the low-intensity interference fell far below threshold, and hence did not contribute to the centroid estimates.

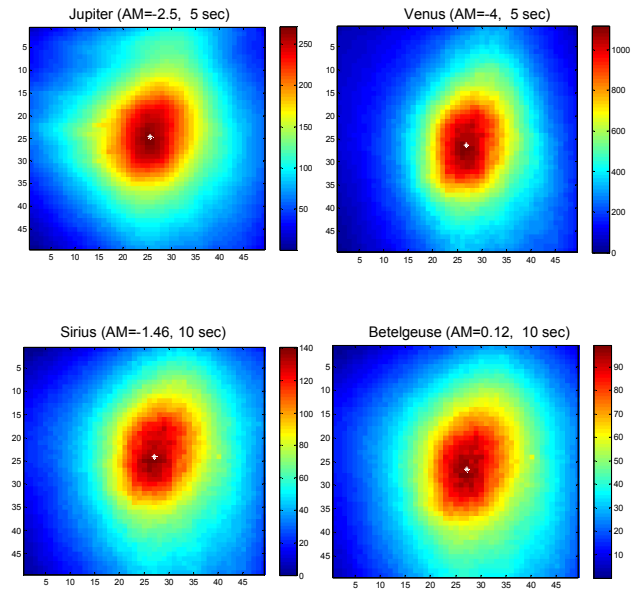

Fig. 8. Threshold-centroid algorithm's estimate of the PSF coordinates, with different sources centered visually over the camera, and recorded on different days at different elevations. Threshold set to 50%.

The importance of real-time tracking to keep the PSF centered over the array is clearly illustrated by the following experiment. The open-loop tracking performance of the 34 meter antenna at DSS-13 for polished panel applications was determined on September 13th , 2012, by first centering the star Vega at high elevation (81.5 degrees), recording the PSF with the FLI camera, then continuing to track Vega as it was setting using only the star's ephemeris and the antenna's RF pointing model. FLI data was recorded after every degree change in elevation. The results are plotted in Fig. 9, where it can be clearly seen that as the star's elevation decreases the PSF wanders away from the initially defined nominal center of the detector array, accumulating large pointing errors that eventually displace the center of the PSF half-way to the detector's edge.

The large accumulated pointing offsets help to justify the use of real-time tracking algorithms, in particular the threshold centroid algorithm described in this article, to keep the PSF centered over the array. Fig. 9 shows that with the tracking algorithm turned off, the pointing error in elevation appears to be linear, accumulating pointing errors as large as 32 mdegs by the time it reaches 57.5 degrees elevation, while the cross-elevation seems to settle between 15-20 mdegs for elevations below 76 degrees. These are very large pointing errors, even for an RF receiver at X-band frequencies, and would eventually degrade the communications performance of the polished panel system. However, by applying real-time pointing estimates every few minutes to correct the pointing drift, the PSF can be kept centered over the array thus providing maximum signal energy for signal detection.

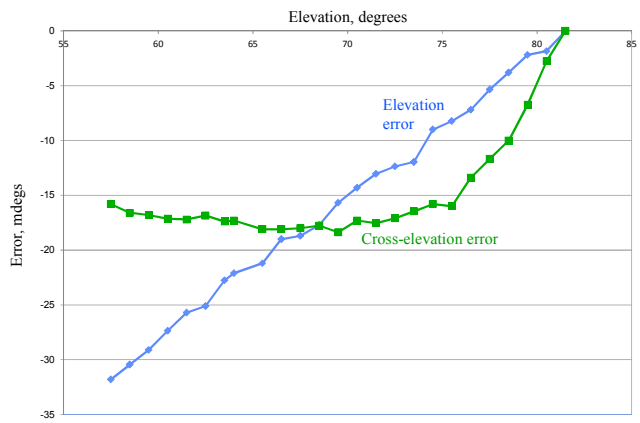

Fig. 9. Open-loop tracking errors accumulated by the polished panel receiver mounted on the 34 meter antenna at DSS-13, while tracking the star Vega.

An example of the algorithm's estimate of the centroid is shown in Fig. 10, where elevation and cross-elevation offsets of ± 50 mdegs were introduced in order to test the algorithm, with the threshold set to 50%. The conversion factor from pixels to angular offset in mdegs was determined empirically, and found to be 4.4 mdegs/pixel along both the elevation and cross-elevation directions.

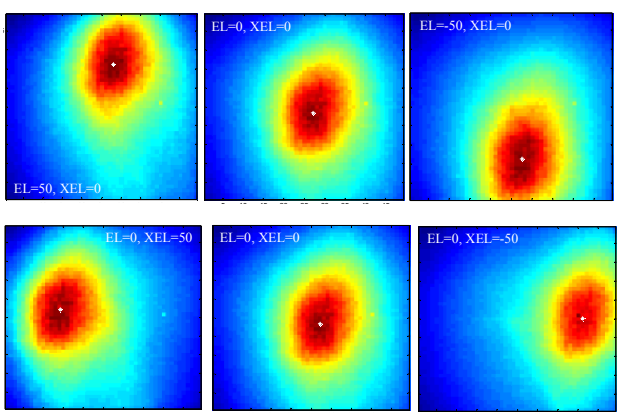

Fig. 10. Threshold centroid algorithm's response to 50 mdeg offsets in elevation and cross-elevation, with the threshold set at 50%. These results were used to estimate the conversion factor from pixels to mdegs: the conversion factor near the middle of the detector array was found to be approximately 4.4, in both the elevation and cross-elevation directions.

Long-exposure PSF estimates were used to evaluate the performance of the tracking algorithm, based on the argument that in any practical high-speed communications system, averaging over time-scales of tens of seconds will provide enough signal energy for a high-intensity image of the PSF. Some coma can be seen above, below and to the sides of the offset PSF, however this does not impact the accuracy of the threshold centroid estimate, which does not respond to low-intensity features that occur below threshold.

Estimates obtained with higher threshold settings, such as 80%, were found to be nearly the same, as can be seen in Fig. 11a. Only after the threshold was lowered to 18.4%, corresponding to the optimum detection threshold shown in Fig. 7, did the centroid estimates begin to differ slightly from the high-threshold estimates, as the slight coma in the lower right of the PSF started to impact these estimates. However, it is evident that all three estimates are close to the center of the array, hence will re-center the PSF adequately in a practical tracking scenario. In fact, the low-threshold setting of 18.4% may turn out to be best for detection applications since it effectively centers the optimum (1, 0) mask (that is, the (1,0) mask that minimizes the average probability of error), particularly in the absence of significant background irregularities or PSF artifacts, but this assertion remains to be shown experimentally.

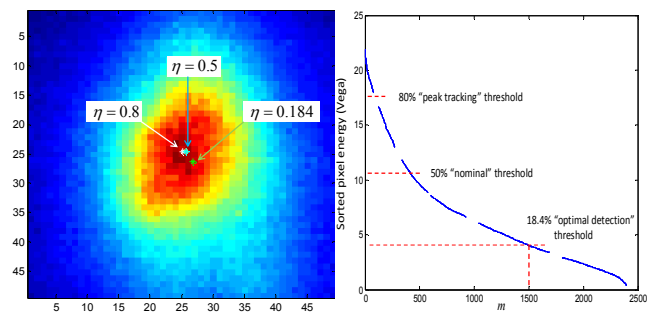

Fig. 11. Dependence of threshold centroid algorithm's estimate on threshold setting: a) response to "peak tracking" 80% threshold; "nominal" 50% threshold; and "optimum detection" 18.4% threshold. b) example of threshold values applied to sorted pixel energies of the upgraded PSF obtained from Vega.

We can see that tracking algorithm performance is not very sensitive to the threshold setting, thus providing the design engineer with viable options to choose the threshold based on other considerations such as complexity or ease of implementation, in a practical communications system.

The response of the 50%-threshold centroid algorithm to applied offsets are shown in Fig. 12, represented as points on the (XEL, EL) plane. The PSF was centered over the sensor visually by applying small pointing offsets to the antenna, and that nominal position was declared to be the center of the coordinate system: (XEL=0, EL=0). Following the centering operation, pointing offsets of $\pm 25, \pm 50$ and ± 100 mdegs were applied to the antenna, and the resulting PSF recorded with the FLI camera while tracking Jupiter. The tracking algorithm was then applied in post-processing, yielding the response shown in Fig. 12. Note that accurate estimates with little cross-coupling were obtained for 50 mdeg and smaller offsets, which is the most important region of the (XEL, EL) plane, since pointing errors tend to develop slowly due to gravitational stress on the antenna's structure, hence it is generally most important to correct for small pointing errors in real-time

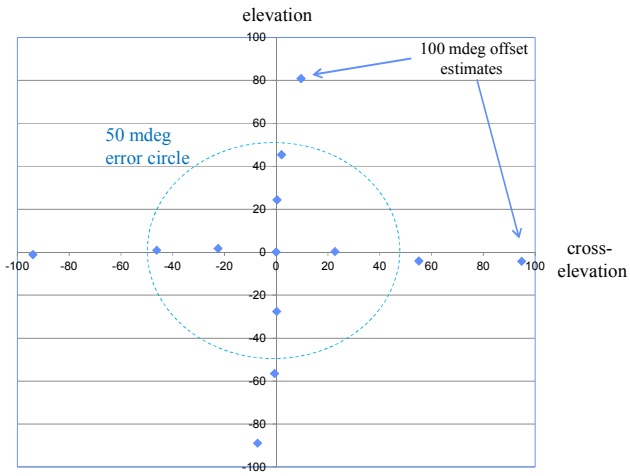

Fig. 12. Response of the threshold-centroid algorithm to offsets of 25, 50, and 100 mdegs in both elevation and cross-elevation directions.

For offsets of 100 mdeg and greater the PSF begins to slide off the sensor, and hence the estimates saturate around 100 mdegs, as can be seen in Fig. 12. In addition, larger cross-coupling can be seen, as the algorithm begins to respond to the tail of the PSF, which may not be as symmetric as the central peak. However, the estimates are still reasonably accurate and in the correct direction, hence will be able to re-center the antenna into the 50 mdeg error circle in a single step, where accurate tracking can take place.

As an application of the approximate lower bounds on centroid estimation error, we consider the Cramer-Rao lower bounds derived in equations (9) and the approximate version for the thresholded estimator given in equation (7). The standard deviation in the y (vertical) direction in the elliptical two-dimensional Gaussian model is the point where the intensity falls to 1/e = 0.368 of its peak value, and similarly in the x (horizontal) direction. The locus of points where the PSF falls to 0.368 of its peak value is the dashed-blue ellipse shown in Fig. 13, with major axis of approximately $44-7=37$ pixels, and minor axis $40-13=27$ pixels, implying that $\sigma_y = 37/2 = 18.5$ pixels and $\sigma_x = 27/2 = 13.5$ pixels. If we assume that the total average signal energy is 150 photons, as in the above examples, then the Cramer-Rao bounds on the coordinate estimates become $\sqrt{\mathrm{var}(\hat{x}_0 - x_0)} = 13.5/\sqrt{150} = 1.1$ and $\sqrt{\mathrm{var}(\hat{y}_0 - y_0)} = 18.5/\sqrt{150} = 1.5$ pixels. The axes of this error ellipse are 2.2 and 3 pixels, as illustrated in Fig. 13 by the dashed-white error ellipse surrounding the white asterisk (the nominal estimate of the centroid, in the absence of background and with zero threshold so that all of the signal energy is used).

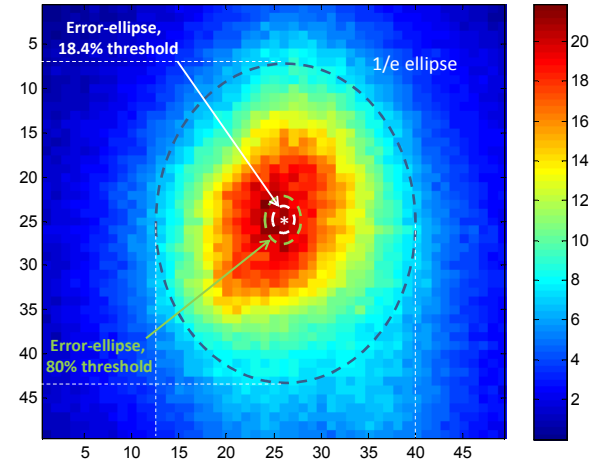

Fig. 13. Standard-deviation ellipse of PSF obtained from the star Vega, used to illustrate the Cramer-Rao bound error-ellipse for low-threshold setting (18.4%), and approximate error-ellipse for high-threshold setting (80%), around the algorithm's estimate of the PSF centroid.

If the tracking threshold is set equal to the optimum detection threshold of 18.4%, thus requiring only a single (1,0) mask for both tracking and signal detection, then 81.6% of the total signal energy is used by the algorithm, and the axes of the error ellipse change by only 10%, yielding an error ellipse only slightly larger than for the ideal case. Even if the threshold is set to the highest value considered here, namely 80%, leaving only 20% of the original signal energy for tracking the centroid, the dimensions of the error ellipse increase by a factor of $\sqrt{5} = 2.2$, yielding $\sqrt{\mathrm{var}(\hat{x}_0^* - x_0)} = 13.5/\sqrt{150/5} = 2.5$ and $\sqrt{\mathrm{var}(\hat{y}_0^* - y_0)} = 18.5/\sqrt{150/5} = 3.4$ pixels, as shown by the dashed-green ellipse in Fig. 13 with axes of 5 and 6.8 pixels. However, this estimate is not very accurate, since the thresholded peak no longer resembles a two-dimensional Gaussian PSF, as assumed in the derivation. But even these approximate results tend to indicate that the error ellipse is much smaller than the extent of the PSF in most cases of interest, leading to accurate tracking and re-centering of the PSF when slowly varying pointing errors are encountered.

6. Summary and Conclusions

Installation, upgrades and initial evaluation of a custom built polished aluminum panel intended for optical communications via hybrid 34-meter DSN antennas has been described in this paper. It was shown that high-quality aluminum panels can be manufactured with surface accuracies sufficient to concentrate light into a small spot that can be detected with large area photon-counting arrays. As part of this demonstration effort, an aluminum panel manufactured by Vertex Antennentechnic GmbH. was installed on the main reflector of the 34-meter antenna at

DSS-13, and a large-sensor camera manufactured by Finger Lakes Instruments was installed into a weather-proof enclosure and mounted next to the subreflector, in order to record the point-spread function (PSF) generated by the polished panel. Data was collected while tracking the planet Jupiter and other bright sources at night, which provided sufficient illumination to produce detailed images of the PSF with various antenna pointing offsets, enabling the evaluation of the polished panel system.

A mathematical model of the focal-plane energy distribution was developed and applied to the experimentally measured PSF in order to predict optical communications and tracking performance. It was noted that significant distortions were present in the PSF when it was first centered over the sensor, the result of mechanical stress on the polished panel introduced by the mounting structure. The panel mounting structure was therefore upgraded to minimize mechanical distortions, resulting in dramatic improvements in the PSF. A practical "threshold-centroid" tracking algorithm was described, its tracking performance estimated via modified Cramer-Rao bounds, and evaluated using the experimentally recorded PSF at DSS-13. It was shown that the performance of the threshold-centroid algorithm did not depend significantly on the threshold setting, thus providing the design engineer with a variety of options for setting the tracking threshold and optimizing detection performance in a practical polished panel optical communications system.

Acknowledgments: The author would like to acknowledge the contributions of team members Daniel Hoppe, Theodore Hanson, Asim Sehic, and Philip Tsao for fabricating and installing the polished panels, camera enclosure and computer interface on the DSS-13 antenna.

The research described in this paper was carried out at the Jet Propulsion Laboratory, California Institute of Technology, under a contract with the National Aeronautics and Space Administration.

REFERENCES

[1] V. Vilnrotter, D. Hoppe, B. Moision, J. Charles, "Optical Communications Performance of Hybrid 34-meter Microwave Antennas," IEEE Aerospace Conference, Big Sky, MT, March 2010.

[2] V. Vilnrotter, "Experimental Evaluation of Optically Polished Panels on the Deep Space Network's 34 Meter Antenna," IEEE Aerospace Conference, Big Sky, MT, March 2012.

[3] V. Vilnrotter, M. Srinivasan, "Adaptive Detector Arrays for Optical Communications Receivers," IEEE Transactions on Communications, Vol. 50, Issue 7, 2002, pp. 1091-1097.

Biographies

Victor A. Vilnrotter *(M'79, SM'02) received his Ph.D. in electrical engineering and communications theory from the University of Southern California in 1978. He joined the Jet Propulsion Laboratory, Pasadena, Calif., in 1979, where he is a Principal Engineer in the Communication Architectures and Research Section. His research interests include electronic compensation of large antennas with focal-plane arrays, adaptive combining algorithms for large antenna arrays, optical communications through atmospheric turbulence, the application of quantum communications to deep-space optical links, and the development of uplink array calibration and tracking technologies. He has published extensively in conferences and refereed journals, and has received numerous NASA awards for technical innovations.*